
Plasma Density Determination from X-Ray Radiography of Laser-Driven Spherical Implosions

The fuel layer density of an imploding spherical shell is inferred from x-ray radiographs. The density distribution is determined by using Abel inversion to compute the radial distribution of the opacity κ from the observed optical depth τ . With the additional assumption of the mass of the remaining cold fuel, the absolute density distribution can be determined. This is demonstrated on the OMEGA Laser System with two x-ray backlighters of different mean energies that lead to the same inferred density distribution independent of backlighter energy.

Recent experiments on the OMEGA laser have successfully inferred the areal density of the imploding capsule at the time of fusion particle production¹⁻³ (hot-spot formation). At this time, the hot-spot temperature is at maximum, whereas the cold main fuel layer is still evolving. The integral areal density of the capsule is determined from the slowing down of protons resulting from D-³He fusion reactions within the fuel. These can be either primary fusion reactions from a D³He gas fill or secondary reactions from a D₂ gas fill. This method determines the total areal density ρR by associating proton energy loss with the amount of plasma traversal. This method is fairly insensitive to the assumptions about the conditions of the plasma but is restricted to sampling the areal density at the time of fusion particle production.

In non-igniting capsules, the cold main fuel layer produces negligible fusion yield; therefore it is difficult to diagnose. The problem is solved by the introduction of an outside source of radiation (backlighter) acting as a probe. Both x-ray⁴ and proton backlighters⁵ have been employed as plasma probes in laser-driven fusion experiments. X-ray backlighters have been extensively used for both planar experiments and spherical implosions on OMEGA.⁶ X-ray backlighting of spherical implosions on OMEGA has been restricted to experiments using fewer than 60 beams to drive the target implosion, freeing up some of the beams to generate the x-ray backlighter emission. The recent completion of the Omega EP Facility⁷ will make it possible to generate a backlighter while using all 60 OMEGA beams to drive the implosion.

In this work it is shown that the density distribution of the plasma can be inferred from framed x-ray radiographs. With x-ray backlighter emission available during and after core formation, the time history of the main fuel layer's density, and therefore the areal density, can be determined. The use of two-dimensional (2-D) imaging techniques such as pinhole imaging, Kirkpatrick-Baez microscopes, and Bragg crystal diffraction are preferred since there may be significant azimuthal variation of the plasma density.

In contrast to a previous treatment of this problem where only the relative density distribution was determined,⁸ it is shown that with the application of Abel inversion and the further constraint of constant mass, the absolute plasma density distribution can be inferred from the framed x-ray radiographs. This is demonstrated using x-ray radiographs of polar-driven implosions⁹ on the OMEGA Laser System⁶ with simultaneous backlighters at a mean energy of ~2.3 keV (from broadband Au emission) and from ~4.7-keV x rays (from a Ti backlighter). Despite a significant difference in the magnitude of the plasma opacity resulting from these two backlighters, the method yields the same density distribution when simultaneous framed images are compared.

Absorption of backlighter x rays along a path L follows the relation

$$I = I_0 \times \exp\left[-\int \mu(E, r)\rho(r)dr\right], \quad (1)$$

where I is the observed intensity, I_0 is the backlighter intensity, μ is the mass absorption coefficient at energy E in cm²/g, and ρ is the density in g/cm³. If the density distribution is spherically symmetric, the integral can be re-expressed as

$$\kappa_A(E, y) = 2 \int_y^\infty \frac{\mu(E, r)\rho(r)rdr}{\sqrt{r^2 - y^2}}, \quad (2)$$

where $\kappa_A(E,y)$ is the Abel transform¹⁰ of the opacity $\kappa(E,r) = \mu(E,r) \rho(r)$ at the projected radial position y . The inverse Abel transform¹⁰ gives the radially dependent opacity

$$\kappa(E,r) = -\frac{1}{\pi} \int_r^\infty \frac{d\kappa_A}{dy} \frac{dy}{\sqrt{y^2 - r^2}}. \quad (3)$$

Normally applied to optically thin emission, Eq. (3), when combined with Eq. (1), determines the radial distribution of the opacity

$$\kappa(E,r) = \frac{1}{\pi} \int_r^\infty \frac{d}{dy} \left\{ \ln \left[\frac{I(y)}{I_0} \right] \right\} \frac{dy}{\sqrt{y^2 - r^2}}. \quad (4)$$

If the mass absorption coefficient is approximately constant through the plasma, as is the case for bound-free absorption¹¹ by inner-shell electrons, then

$$\rho(r) = \kappa(E,r) / \mu_{\text{eff}}(E), \quad (5)$$

where $\mu_{\text{eff}}(E)$ is the mass absorption coefficient averaged over the effective energy band of the radiograph. Because of uncertainties in the instrumental response or an incomplete knowledge of the spectral shape, it is difficult to determine the exact value of $\mu_{\text{eff}}(E)$. If, however, the mass of the plasma shell M_{shell} is assumed or obtained from simulations, then $\mu_{\text{eff}}(E)$ can be determined as follows:

$$M_{\text{shell}} = \int \rho(r) dV = 4\pi \int \frac{\kappa(E,r)}{\mu_{\text{eff}}(E)} r^2 dr, \quad (6)$$

$$\therefore \mu_{\text{eff}}(E) = \frac{4\pi}{M_{\text{shell}}} \int \kappa(E,r) \times r^2 dr. \quad (7)$$

By choosing M_{shell} to be the unablated mass, the absolute density is then determined. The applicability of this approximation has been previously explored¹² for deuterated polystyrene (CD) and shown to apply for absorption by the carbon atoms in the polystyrene when the temperature of the absorber is below ~ 100 eV and the density is below ~ 10 g/cm³. If the plasma is isothermal, the temperature restriction is further relaxed. Fujioka *et al.*¹³ have shown that absorption of x rays from a Ti backlighter (one of two used in this work) by polystyrene (CH) can indeed be characterized by an effective energy-band-dependent absorption coefficient.

If the absorber is fully stripped, as is the case for a pure-hydrogen fuel layer, and is at a sufficiently high temperature, as would be expected for a D or DT main fuel layer near stagnation, the opacity is $\propto \rho^2/T^{1/2}$, and, therefore, the optical depth is $\propto \rho^2 R/T^{1/2}$ (Refs. 14 and 15), where T is the temperature and R is the radius. If the temperature variation of the absorber is small, the radial variation of the opacity can be determined by Abel inversion from which a functional form of the density distribution can be determined. The assumption of constant mass allows one to calculate the absolute density distribution as a function of radius.

Experiments were performed using 40 beams of the OMEGA laser in the polar-drive illumination configuration,⁹ emulating the conditions on the NIF (the National Ignition Facility)¹⁶ when direct-drive implosions are performed with the beams in the indirect-drive configuration. The beam pointing used was described in Marshall *et al.*⁹ (case 3, with offsets of rings 1, 2, and 3 of 90, 150, and 150 μm , respectively) on a target with an outer radius of 433 μm . The target consisted of a 24- μm -thick glow-discharge-polymer (GDP) (i.e., CH) shell filled with 15 atm of D₂ at room temperature. The main drive pulse consisted of a 1.5-ns pulse with a 1-to-3 (foot-to-main) intensity ratio, with the foot and main part of the pulse having approximately equal durations (~ 0.75 ns). A total of 13.2 kJ was incident on the target with 1-THz-bandwidth smoothing by spectral dispersion (SSD)¹⁷ with polarization smoothing¹⁸ used to minimize small-scale illumination nonuniformities. This pulse shape was used to keep the main fuel layer on a low adiabat ($E/E_{\text{Fermi}} \sim 3$) (Ref. 19).

Two backlighter targets were employed opposite two x-ray framing cameras. One backlighter was a 25- μm -thick Au foil and the other a 25- μm -thick Ti foil, each with four OMEGA beams of ~ 350 J/beam, focused to diameters of 750 μm and 600 μm , respectively. Each framing camera was positioned behind a 4×4 array of 10- μm -diam pinholes producing four strips of framed images with a time-gated resolution of ~ 30 ps, 56 ps between images, and strip times independently set to the nearest 100 ps. Absolute frame times were determined by observing the backlighter onset on the first strip and from the measured delay from strip to strip determined from an electronically recorded monitor signal.

The images are recorded on film with an imposed step wedge, so that absolute intensity variations can be determined. The exposed images and step wedge are developed simultaneously to make possible the subsequent conversion to intensity

variation from scanned and digitized film. Variations of the backlighter intensity are removed by fitting the shape of the backlighter to a supergaussian-plus background outside the region of the target radiograph and then extending this fit to the region of the radiograph.²⁰

Figure 117.24 shows a set of these corrected radiographs up to shell stagnation, which occurs at ~ 2.3 ns. The values are presented as $-\ln(I/I_0)$ [i.e., the optical depth τ]; all values are >0 with the exception of the frames from 2.32 ns and on, where self-emission from the core exceeds emission from the backlighter in the central region of the images. Figure 117.25(a) shows the azimuthally averaged optical-depth variation for one nearly simultaneous pair (at the mean time of $t = 2.14$ ns) of Au- and Ti-backlit images. The magnitude of the optical depth is greater for the lower-energy backlighter, as expected. The dotted line in Fig. 117.25(a) is the Au-backlit profile divided by 1.7, showing that the optical depths differ by only a multiplicative constant. Applying Abel inversion and assuming the unablated shell mass (3.34×10^{-5} g) given by the one-dimensional (1-D) hydrodynamic code *LILAC*²¹ determines the density distributions from the observed optical depths [Fig. 117.25(b)]. The inferred density distributions from the Au and Ti backlighters are nearly identical, with only small differences due to noise in the images.

Figure 117.26 shows the density distributions determined for a sample of these images. The densities inferred from one

additional simultaneous pair of Au- and Ti-backlit images are included. The *LILAC*-simulated shell density is shown for comparison for the 2.20-ns case. Figure 117.27 shows the resulting calculated shell areal densities ρR_{shell} determined from all Au- and Ti-backlit images plotted as a function of frame time from the beginning of the main laser pulse ($t = 0$). For the two frames where the Au- and Ti-backlit images occurred at the same time, the areal density values are the same within errors. All times have an uncertainty of ± 50 ps. The absolute densities, and therefore areal densities, are assumed to be uncertain by $\pm 10\%$ because of an uncertainty in the unablated mass. The time from ~ 2.3 to 2.6 ns corresponds to the time during which intense x-ray emission from the core as well as fusion production occurs. During peak emission, heat from the core moves out through the shell and absorption by the backlighter is momentarily obscured. Since an independent measurement of this emission is not available (image with no backlighter), it cannot be corrected for and no density profiles are determined during this time interval. Later in time, the shell cools and absorption of the backlighter reappears. Frames during this later time were recorded by the Ti-backlit framing camera (2.70 ns and later).

The mean neutron production time (bang time), as recorded by the neutron temporal diagnostic,²² occurred at 2.43 ns during the time interval when x-ray emission from the core is evident. The areal density averaged over the time of fusion particle production was independently determined by a set of three filtered

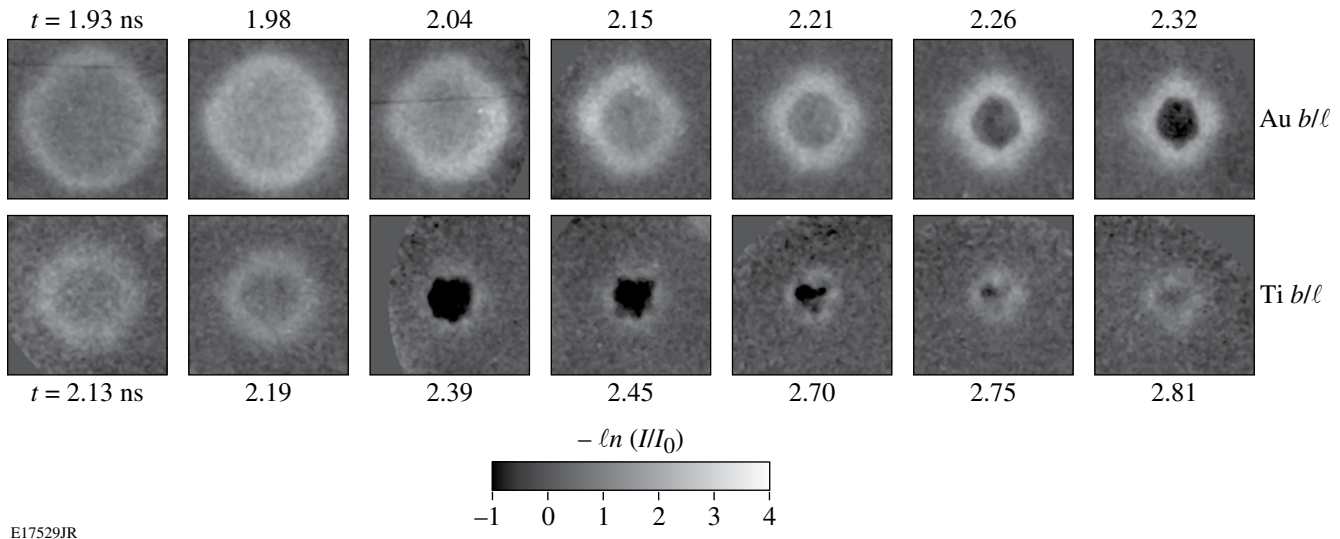


Figure 117.24
Intensity-corrected x-ray radiographs from OMEGA shot 49331 taken with two x-ray framing cameras, one backlit by an Au target and the other by a Ti target. Each image is a $400 \times 400\text{-}\mu\text{m}$ region corrected for backlighter intensity variation as explained in the text.

CR39 packs measuring the slowing down of the $D-^3He$ protons¹ and yields a value of $\langle \rho R \rangle_p = 58 \pm 5 \text{ mg/cm}^2$ (the error is one standard deviation of the three values). The value determined in this case is the sum of the areal densities of the fuel (gas fill) and the shell. An estimate of the fuel areal density ρR_{fuel} is determined from the size of the observed core emission at stagnation ($\sim 50 \text{ }\mu\text{m}$) and mass conservation, yielding $\rho R_{\text{fuel}} = 6 \pm 1 \text{ mg/cm}^2$. The proton inferred shell areal density is therefore $\langle \rho R_{\text{shell}} \rangle_p = 52 \pm 5 \text{ mg/cm}^2$ and is plotted as a single point in Fig. 117.27 at bang time. The value determined from the proton spectra falls closely on the trend of the x-ray measurements, giving additional credence to the results of this method. The *LILAC* simulation of this implosion was performed assuming flux-limited diffusion²³

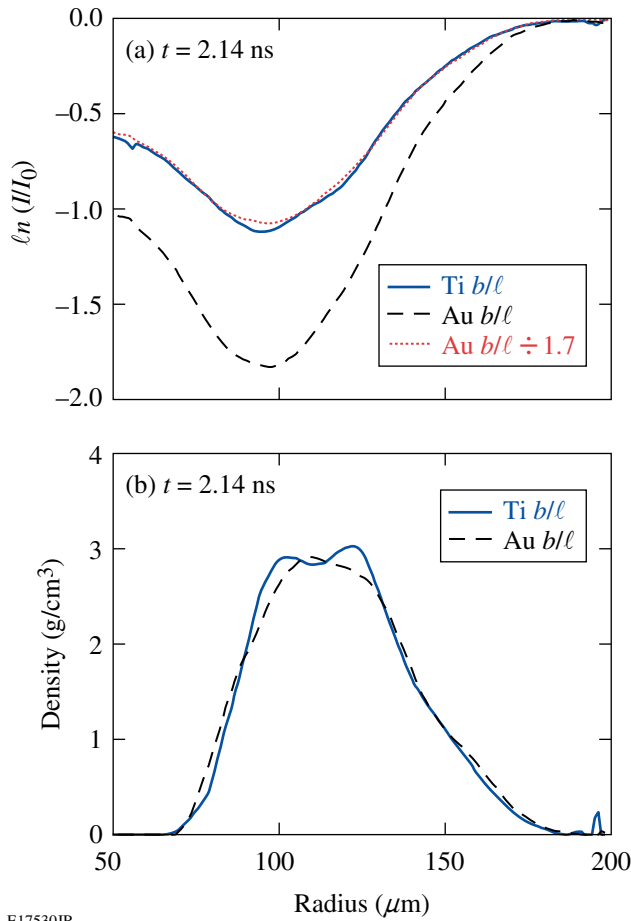


Figure 117.25 (a) The natural logarithm of the intensity variation as a function of projected radial distance in the image plane for a simultaneous pair of Au- and Ti-backlit images. The profiles are azimuthally averaged about the image centers. The dotted line is the Au profile normalized to the Ti profile, demonstrating that they differ only by a multiplicative constant (1.7). (b) The absolute density distributions were computed from the intensity profiles of (a) by Abel inversion with the additional constraint of constant mass as described in the text.

with a flux limiter $f = 0.06$. The predicted areal density is shown as a solid line in Fig. 117.27. The areal density measurements are seen to closely follow this prediction until the time of stagnation, where significant departures from spherical symmetry can be seen in the framed images (Fig. 117.24).

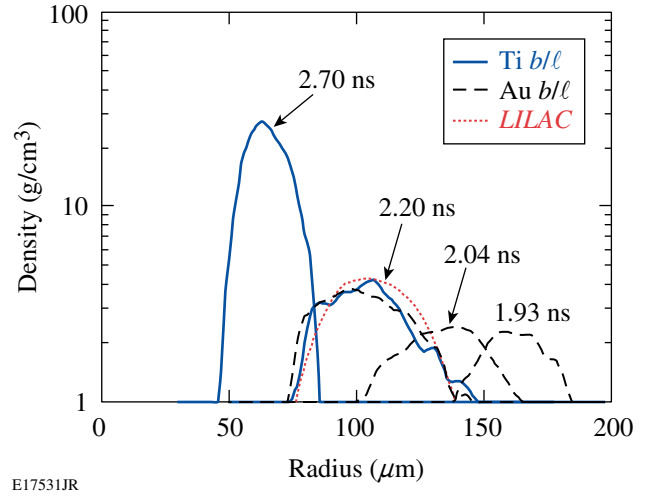


Figure 117.26 Density distributions computed from the x-ray radiographs showing the evolution of the shell density and position as a function of the indicated frame times.

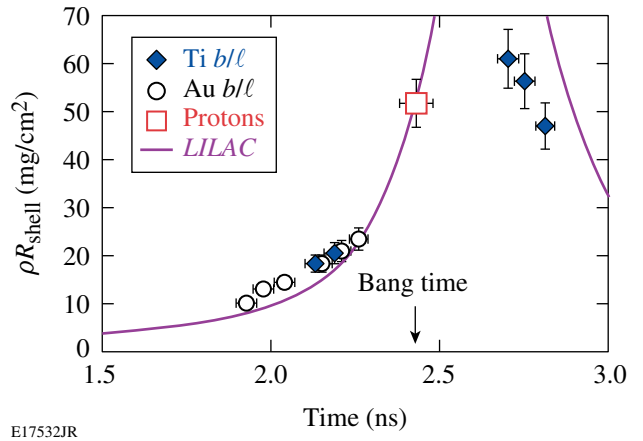


Figure 117.27 The shell areal densities computed from all available x-ray radiographs including those where the emission from the core is just starting (2.3 ns) to the tail end of the core emission (2.6 ns) and later. The value determined from the proton spectra is plotted at the time of peak neutron emission (2.43 ns). The *LILAC*-simulated shell areal density, shown as a solid curve, reached a peak of 110 mg/cm^2 at 2.64 ns (off scale).

This analysis demonstrates that with the application of an area x-ray backlighter, the time history of the shell areal density can be measured on a single implosion experiment from early in the implosion, up to stagnation, and again later in time after core emission has subsided. Such a determination is limited by the temporal extent of the backlighter and the requisite exclusion of target self-emission. A similar measurement of the areal-density time history using proton radiography⁵ requires that the implosion be repeated, acquiring a single time measurement from each of a series of identical implosions. The x-ray radiography technique therefore offers a much less intensive use of the experimental facility, not requiring that the implosion be repeated multiple times to acquire the areal-density time history. The results of this technique support the conclusion that the direct-drive implosion exhibits near 1-D performance, in this case up to the time of core self-emission, with evolving nonuniformities affecting the performance thereafter.

ACKNOWLEDGMENT

This work was supported by the U.S. Department of Energy Office of Inertial Confinement Fusion under Cooperative Agreement No. DE-FC52-08NA28302, the University of Rochester, and the New York State Energy Research and Development Authority. The support of DOE does not constitute an endorsement by DOE of the views expressed in this article.

REFERENCES

1. F. H. Séguin, J. A. Frenje, C. K. Li, D. G. Hicks, S. Kurebayashi, J. R. Rygg, B.-E. Schwartz, R. D. Petrasso, S. Roberts, J. M. Soures, D. D. Meyerhofer, T. C. Sangster, J. P. Knauer, C. Sorce, V. Yu. Glebov, C. Stoeckl, T. W. Phillips, R. J. Leeper, K. Fletcher, and S. Padalino, *Rev. Sci. Instrum.* **74**, 975 (2003).
2. V. A. Smalyuk, P. B. Radha, J. A. Delettrez, V. Yu. Glebov, V. N. Goncharov, D. D. Meyerhofer, S. P. Regan, S. Roberts, T. C. Sangster, J. M. Soures, C. Stoeckl, J. A. Frenje, C. K. Li, R. D. Petrasso, and F. H. Séguin, *Phys. Rev. Lett.* **90**, 135002 (2003).
3. J. A. Frenje, C. K. Li, F. H. Séguin, J. Deciantis, S. Kurebayashi, J. R. Rygg, R. D. Petrasso, J. Delettrez, V. Yu. Glebov, C. Stoeckl, F. J. Marshall, D. D. Meyerhofer, T. C. Sangster, V. A. Smalyuk, and J. M. Soures, *Phys. Plasmas* **11**, 2798 (2003).
4. O. L. Landen *et al.*, *Rev. Sci. Instrum.* **72**, 627 (2001).
5. C. K. Li, F. H. Séguin, J. A. Frenje, M. Manuel, R. D. Petrasso, V. A. Smalyuk, R. Betti, J. Delettrez, J. P. Knauer, F. Marshall, D. D. Meyerhofer, D. Shvarts, C. Stoeckl, W. Theobald, J. R. Rygg, O. L. Landen, R. P. J. Town, P. A. Amendt, C. A. Back, and J. D. Kilkenny, *Plasma Phys. Control. Fusion* **51**, 014003 (2009).
6. T. R. Boehly, D. L. Brown, R. S. Craxton, R. L. Keck, J. P. Knauer, J. H. Kelly, T. J. Kessler, S. A. Kumpan, S. J. Loucks, S. A. Letzring, F. J. Marshall, R. L. McCrory, S. F. B. Morse, W. Seka, J. M. Soures, and C. P. Verdon, *Opt. Commun.* **133**, 495 (1997).
7. C. Stoeckl, J. A. Delettrez, J. H. Kelly, T. J. Kessler, B. E. Kruschwitz, S. J. Loucks, R. L. McCrory, D. D. Meyerhofer, D. N. Maywar, S. F. B. Morse, J. Myatt, A. L. Rigatti, L. J. Waxer, J. D. Zuegel, and R. B. Stephens, *Fusion Sci. Technol.* **49**, 367 (2006).
8. D. H. Kalantar *et al.*, *Rev. Sci. Instrum.* **68**, 814 (1997).
9. F. J. Marshall, R. S. Craxton, M. J. Bonino, R. Epstein, V. Yu. Glebov, D. Jacobs-Perkins, J. P. Knauer, J. A. Marozas, P. W. McKenty, S. G. Noyes, P. B. Radha, W. Seka, S. Skupsky, and V. A. Smalyuk, *J. Phys. IV France* **133**, 153 (2006).
10. R. N. Bracewell, *The Fourier Transform and Its Applications*, 3rd ed. (McGraw-Hill, Boston, 2000), pp. 351–356.
11. H. A. Bethe and E. E. Salpeter, *Quantum Mechanics of One- and Two-Electron Atoms* (Academic Press, New York, 1957), pp. 295–305.
12. F. J. Marshall, J. A. Delettrez, R. Epstein, and B. Yaakobi, *Phys. Rev. E* **49**, 4381 (1994).
13. S. Fujioka *et al.*, *Phys. Plasmas* **10**, 4784 (2003).
14. Ya. B. Zel'dovich and Yu. P. Raizer, in *Physics of Shock Waves and High-Temperature Hydrodynamic Phenomena*, edited by W. D. Hayes and R. F. Probstein (Academic Press, New York, 1966), Chap. V, Vol. I, pp. 269–272.
15. B. Yaakobi, R. Epstein, and F. J. Marshall, *Phys. Rev. A* **44**, 8429 (1991).
16. W. J. Hogan, E. I. Moses, B. E. Warner, M. S. Sorem, and J. M. Soures, *Nucl. Fusion* **41**, 567 (2001).
17. S. Skupsky, R. W. Short, T. Kessler, R. S. Craxton, S. Letzring, and J. M. Soures, *J. Appl. Phys.* **66**, 3456 (1989).
18. T. R. Boehly, V. A. Smalyuk, D. D. Meyerhofer, J. P. Knauer, D. K. Bradley, R. S. Craxton, M. J. Guardalben, S. Skupsky, and T. J. Kessler, *J. Appl. Phys.* **85**, 3444 (1999).
19. J. D. Lindl, *Phys. Plasmas* **2**, 3933 (1995).
20. J. P. Knauer, R. Betti, D. K. Bradley, T. R. Boehly, T. J. B. Collins, V. N. Goncharov, P. W. McKenty, D. D. Meyerhofer, V. A. Smalyuk, C. P. Verdon, S. G. Glendinning, D. H. Kalantar, and R. G. Watt, *Phys. Plasmas* **7**, 338 (2000).
21. J. Delettrez, R. Epstein, M. C. Richardson, P. A. Jaanimagi, and B. L. Henke, *Phys. Rev. A* **36**, 3926 (1987).
22. R. A. Lerche, D. W. Phillion, and G. L. Tietbohl, *Rev. Sci. Instrum.* **66**, 933 (1995).
23. R. C. Malone, R. L. McCrory, and R. L. Morse, *Phys. Rev. Lett.* **34**, 721 (1975).